CrossMark click for updates

Astrocytes regulate cortical state switching in vivo

Kira E. Poskanzer[a,1,2] and Rafael Yuste[a]

[a]Department of Biological Sciences, Columbia University, New York, NY 10027

Edited by Charles F. Stevens, The Salk Institute for Biological Studies, La Jolla, CA, and approved March 18, 2016 (received for review October 20, 2015)

The role of astrocytes in neuronal function has received increasing recognition, but disagreement remains about their function at the circuit level. Here we use in vivo two-photon calcium imaging of neocortical astrocytes while monitoring the activity state of the local neuronal circuit electrophysiologically and optically. We find that astrocytic calcium activity precedes spontaneous circuit shifts to the slow-oscillation–dominated state, a neocortical rhythm characterized by synchronized neuronal firing and important for sleep and memory. Further, we show that optogenetic activation of astrocytes switches the local neuronal circuit to this slow-oscillation state. Finally, using two-photon imaging of extracellular glutamate, we find that astrocytic transients in glutamate co-occur with shifts to the synchronized state and that optogenetically activated astrocytes can generate these glutamate transients. We conclude that astrocytes can indeed trigger the low-frequency state of a cortical circuit by altering extracellular glutamate, and therefore play a causal role in the control of cortical synchronizations.

astrocyte | cortex | slow oscillation | calcium imaging | glutamate

The neocortical slow oscillation (~1 Hz) that defines slow-wave sleep (SWS) is believed to play a critical role in memory consolidation by coordinating cell assemblies in areas within and outside the cortex (1–4). This cortical state is in marked contrast to rapid-eye-movement (REM) sleep and wakefulness, which are dominated by low-amplitude and high-frequency cortical activity (5). Slow cortical rhythms are also observed during the waking state, as well as during sleep (6–10), suggesting widespread functional roles for this oscillation. Although the slow oscillation is cortically generated (11–14), the circuit mechanisms that drive the cortex into the slow-wave state remain unclear. Because neuronal responses to external stimuli are modulated by brain state, the mechanisms that drive transitions to different states—the relatively synchronized, slow-oscillation–dominated state or the desynchronized, more "awake" or attentive state—have recently been of intense interest, although most of these have focused on the shift to the desynchronized state (15–19). These studies have critically examined the effects of neuronal and sensory manipulations on brain state and the effects of brain state on processing, but have not investigated how other cellular circuit components may influence these states.

Astrocytes have been implicated in SWS and the regulation of UP states—the cellular underpinnings of the slow oscillation (20–23)—and are attractive candidates for carrying out a widespread circuit role because each astrocyte has the potential to influence thousands of synapses simultaneously (24). However, the methodology used to demonstrate an astrocyte-specific function in regulation of SWS (21) and the slow oscillation (22) has become controversial (25, 26), leaving astrocytes' role in the generation of the slow-oscillation state uncertain. In addition, there are few data on astrocytes' roles in acute changes in brain state, as these previous in vivo studies of oscillations have used longer-term, transcription-based manipulations of astrocyte function (21, 22, 27). And although astrocytic activity may be acutely shaped by neuromodulatory signals similar to neurons during brain state changes (28, 29), these effects do not specifically address the causal role that astrocytes may play in these shifts. Therefore, the physiological role of astrocytes in these state switches remains an open question.

One reason the roles of astrocytes in circuit functions remain unclear is that their complex Ca^{2+} spatiotemporal dynamics are just beginning to be understood, in terms of activation and output. Because astrocytes are minimally electrically active, understanding their activity via Ca^{2+} dynamics is particularly important, and recent advances in Ca^{2+} imaging tools have enabled Ca^{2+} monitoring throughout the entire astrocyte and not only in the soma (29–32). Indeed, in recent slice and in vivo experiments, it has been shown that most of the Ca^{2+} activity in astrocytes occurs in the processes, and not in the somata (32–35). At the same time, in most previous studies of population astrocyte Ca^{2+} signaling, bulk-loaded dyes have been used, which only load the somata and the primary branches (36). Although this has led to the reinterpretation of many studies only showing Ca^{2+} changes in the somata, few studies have yet investigated the relationship between physiological astrocyte Ca^{2+} activity and the neural circuit in vivo. Thus, the function of astrocyte activity in the neocortical circuit and its reciprocal relationship with neurons are still poorly understood.

In this current study, we monitor the activity of populations of cortical astrocytes in vivo (37) and simultaneously record neurons either electrophysiologically or with Ca^{2+} imaging. We uncover a temporal relationship between spontaneous astrocyte Ca^{2+} activity and the shift to the slow-oscillation state in vivo. To manipulate astrocytic Ca^{2+} activity, we use an optogenetic tool, Archaerhodopsin (Arch), to increase intracellular Ca^{2+} concentration ($[Ca^{2+}]_i$) in astrocytic processes in a light-dependent manner. This manipulation shifts the cortical circuit into a slow-oscillation regime and increases coactive neuronal firing. We explore the mechanism of this astrocyte-generated cortical state switch and find that "spikes" in extracellular glutamate around astrocytes co-occur with shifts to the slow-oscillation state and that Arch stimulation of astrocytes can generate these local extracellular glutamate spikes. Thus, astrocyte activity can regulate the shift to the slow cortical oscillation state, thereby acutely regulating the state of a neural circuit.

Significance

Astrocytes—a type of glial cell—and neurons function together in neural circuits, but how astrocytes affect circuit function remains poorly understood. By measuring the fluorescent calcium activity of astrocytes while recording the electrophysiological oscillations in the mouse cortex, we find that astrocytes, through regulation of extracellular glutamate, are involved in triggering a slow neuronal rhythm in the brain that has been shown to be important in sleep and memory formation.

Author contributions: K.E.P. and R.Y. designed research; K.E.P. performed research; K.E.P. analyzed data; and K.E.P. wrote the paper.

The authors declare no conflict of interest.

This article is a PNAS Direct Submission.

Freely available online through the PNAS open access option.

[1]Present address: Department of Biochemistry & Biophysics, University of California, San Francisco, CA 94143.

[2]To whom correspondence should be addressed. Email: kira.poskanzer@ucsf.edu.

This article contains supporting information online at www.pnas.org/lookup/suppl/doi:10.1073/pnas.1520759113/-/DCSupplemental.

Results

Simultaneous Recording of Cortical Astrocyte Ca^{2+} Activity and Local Field Potential in Vivo. To explore the relationship between cortical astrocyte signaling and spontaneous neuronal network activity in vivo, we first expressed the genetically encoded Ca^{2+} indicator GCaMP6s (31) specifically in cortical astrocytes with a viral targeting strategy (*AAV1-CAG.FLEX-GCaMP6s* into an hGFAP-Cre mouse; Fig. 1 *A* and *B*, Fig. S1, and Movie S1). We used two-photon in vivo imaging of layer (L)2/3 astrocytes in the primary visual cortex (V1) of urethane-anesthetized mice to measure Ca^{2+} dynamics throughout astrocytes, as has previously been demonstrated in slice preparations (33) and in vivo without affecting astrocytic GFAP expression (38). Using coexpression of GCaMP6 and tdTomato in cortical astrocytes, we confirmed that temporally variable spontaneous Ca^{2+} transients (Fig. 1 *C* and *D*) reflect changes throughout the soma and processes of astrocytes (Fig. 1 *E–H* and Movie S2; mean Ca^{2+} event duration 15.7 ± 0.83 s and amplitude 0.61 ± 0.02 d*f*/*f*). We also confirmed that virus injection and expression of GCaMP and the other viruses used in this study resulted in similar levels of astrocytic GFAP expression in the cortex via immunohistochemistry, indicating that effects we observe are due to experimental manipulations and not to astrocyte reactivity (39, 40) (Fig. S1 *C–H*). The majority of astrocytic Ca^{2+} transients were observed in the processes rather than the soma [85.6 ± 2.6% of active regions of interest (ROIs) and 86.7 ± 3.2% of Ca^{2+} transients in processes; Fig. 1 *E* and *F*], as previously observed (29, 32–34). The observed astrocytic spatiotemporal Ca^{2+} dynamics were distinct from those observed in neurons after specific neuronal expression of GCaMP6s in neurons in cortical L2/3, as previously demonstrated (31) (Movie S3).

While imaging Ca^{2+} dynamics, we recorded local field potential (LFP) activity from cortical L2/3 and observed spontaneous alternations in brain state every 5.4 ± 0.37 min (Fig. 1*I*; $n = 7$ animals, 11 30-min trials), closely resembling the switch between REM and SWS (41–44). This spontaneous switch from a high to low frequency-dominated state, characterized by the clear presence of UP and DOWN states of the slow oscillation and a decrease in the power of frequencies above 2 Hz, has been well-described previously in both awake animals and under various types of anesthesia (7, 41–44) (Fig. 1 *I* and *J* and Fig. S1 *I–K*), indicating that this is a generalized, essential feature of cortical circuits.

Astrocyte Ca^{2+} Activity Changes with State Shifts. By simultaneously recording LFP and astrocyte Ca^{2+} activity, we noticed a clear temporal relationship between brain state shift and the average astrocyte Ca^{2+} activity (Fig. 2 *A–E* and Fig. S2*H*). To quantify this relationship, we automatically detected average astrocyte Ca^{2+} increases (gray), and increases (red) and decreases (pink) in a low-frequency LFP band (0.5–2 Hz), marking automatically detected "events" above/below a threshold (Figs. 1*J* and 2*F* and *Materials and Methods*). We plotted the closest LFP event to every astrocyte Ca^{2+} event in each 5-min trial (Fig. 2*G*). The average shifts to a low frequency-dominated state were tightly distributed, following the astrocyte Ca^{2+} activation by 11.2 ± 2.6 s (Fig. 2 *F–I*, red and Fig. S2 *A* and *B*; $n = 5$ animals, 22 5-min trials), whereas shifts in the opposite direction, away from the slow-oscillation state (pink), occurred at 14.1 ± 11.2 s but were more broadly distributed around the Ca^{2+} event mean (Fig. 2 *G* and *H*; two-sample *F* test). Similarly, low-frequency increases were more tightly distributed than high-frequency decrease

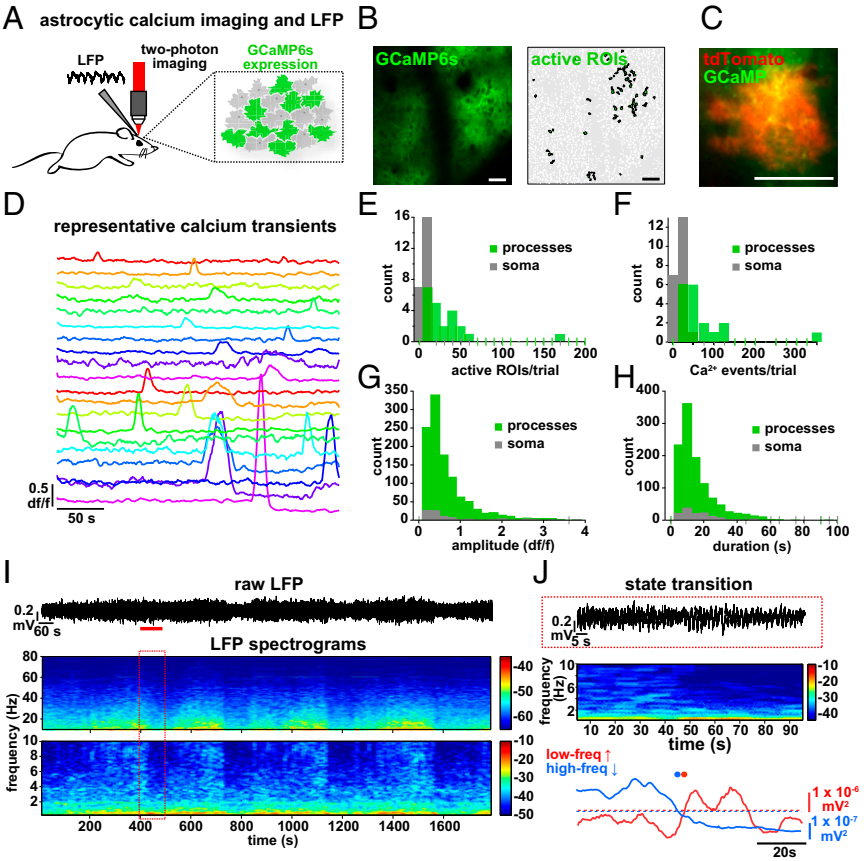

Fig. 1. Simultaneous in vivo Ca^{2+} imaging of cortical astrocytes with GCaMP6s and LFP recording of the local cortical state. (*A*) Experimental setup. Injection of *AAV1-CAG.FLEX-GCaMP6s* into GFAP-Cre mice results in GCaMP6s expression in a subset of cortical astrocytes and allows two-photon imaging and LFP recording. (*B*, *Left*) Expression of GCaMP6s in L2/3 of V1. Note the low baseline fluorescence, as is typical for GCaMP6s (31). (*B*, *Right*) Active ROIs from a 5-min movie of an imaging field (Movie S1). (*C*) Coexpression of GCaMP6s and tdTomato in a single astrocyte demonstrates expression of both fluorescent proteins throughout the astrocyte (Movie S2). [Scale bars, 50 μm (*B* and *C*).] (*D*) d*f*/*f* Ca^{2+} traces from 20 representative ROIs in *B*. Note the heterogeneity of the amplitude and duration of transients. (*E–H*) Statistics for Ca^{2+} imaging experiments in Fig. 2 ($n = 22$ 5-min trials). (*E*) Distribution of subcellular localization of active ROIs per 5-min trial. Distribution of the number of Ca^{2+} events per experiment for all active ROIs (*F*) and amplitude (*G*) and duration (*H*) of all Ca^{2+} transients. ROIs from astrocyte somata are shown in gray and from processes are shown in green. (*I*) Raw LFP data of a 30-min recording in L2/3 of the cortex (*Top*) and resulting spectrograms calculated from raw LFP, separated into low (0.25–10 Hz) and high (10–80 Hz) graphs for clarity. Note the periodic state switching from the high frequency-dominated to the low frequency-dominated state. The red box corresponds to 100 s of LFP, marked by a red line in the raw trace. In spectrograms here and throughout paper, color bars are in units of 10*log(mV^2). (*J*) Example of a state transition from a 100-s sample (red line) in *I*, with raw data (*Top*), spectrogram (*Middle*), and traces quantifying the power in low- and high-frequency bands (*Bottom*). Automatically detected increases in the low-frequency band above threshold (red dots) and decreases in the high-frequency band below threshold (blue dots) are plotted to emphasize the state transition to a slow-oscillation state.

events (3–10 Hz; Fig. 2 *F* and *I*, blue and Fig. S2 *A–D*; two-sample *F* test), although these events were also clustered around the astrocyte Ca^{2+} events (mean −23.9 ± 7.9 s), demonstrating that the switch to the low frequency-dominated state is often (as in Fig. 2 *C–F*), but not always, accompanied or preceded by a decrease in the high-frequency power. We did not uncover a similar relationship when examining frequency bands higher than 10 Hz (Fig. S2*H*), but we do see clustering of astrocyte Ca^{2+} events before shifts to the low-frequency state when we calculate Ca^{2+} events from the LFP event, rather than the inverse, as in Fig. 2 *G* and *H* (Fig. S2 *E–G*). The close temporal relationship between astrocyte Ca^{2+} and a shift to the slow-oscillation state was evident whether the individual Ca^{2+} transients were synchronized across the imaging field or not (Fig. 2*D*, Fig. S3 *A–E*, and Movie S4). In addition, similar results were obtained using a faster GCaMP probe that is trafficked to the membrane of astrocyte processes [Fig. S3 *F–J*, *Lck-GCaMP6f* (33) and Movie S5], demonstrating a relationship between neuronal network state switches in the cortex and astrocyte signaling whereby Ca^{2+} increases in the population of L2/3 astrocytes precede shifts to a synchronized, slow-oscillation–dominated regime.

Using Optogenetics to Drive Ca^{2+} Increases in Astrocyte Processes. To test whether there is a causal relationship between astrocyte activity and brain state, we manipulated astrocyte Ca^{2+} activity and observed its effects on the neural circuit by using a previously unidentified method for specific optogenetic activation of astrocytes with Arch, a tool normally used to inhibit neurons by pumping H^+ out of the cell (45). Viral injection of *CAG.FLEX-Arch-GFP* into a GFAP-Cre mouse resulted in astrocyte-specific expression of Arch-GFP, based on astrocytes' highly and finely branched morphology that distinguishes them from neuronal and other glial cell types (Fig. 3 *A* and *B*). To confirm the morphological observation of expression, we also pressure-injected rhod-2 AM, a Ca^{2+} indicator that specifically loads astrocytes (46), into the cortex and observed that the somata of the Arch-GFP^+ cells were clearly labeled with rhod-2 and that the Arch-GFP^+ processes wrapped around vasculature, as is typical for these cells (Fig. 3 *A* and *B*). In slice experiments, whole-cell patch clamping of Arch-GFP^+ cells and subsequent presentation of yellow light flashes confirmed Arch expression due to the resultant hyperpolarization (−1.37 ± 0.04-mV shift; $n = 28$; Fig. 3*C*). To test whether Arch activation increases intracellular Ca^{2+} concentration in astrocytic branches in a physiological manner in vivo, we coexpressed Arch-tdTomato and GCaMP6s in astrocytes. Double viral injection of Arch-tdTomato and GCaMP6s results in a patchwork of astrocytic expression in the cortex in vivo, with astrocytes labeled with either one of these proteins or with both (mean 3.75 ± 1.9 $Arch^+$, 1.75 ± 0.9 $Arch^+$/$GCaMP^+$ cells per field; Fig. 3 *D* and *E*). In cells expressing both proteins, we could image Ca^{2+} dynamics before and after Arch activation, and found that light stimulation of $Arch^+$ astrocytes consistently evoked Ca^{2+} transients in branches with durations of the same length, and amplitudes slightly decreased, compared with ongoing spontaneous activity in interleaved no-stim control trials (Fig. 3 *F–H* and Fig. S4 *A–D*; $n = 4$ animals, 16 trials, 571 Ca^{2+} events; peak Ca^{2+} response 18.2 ± 2.6 s after stimulus; mean duration 13.9 ± 0.49 s and amplitude 0.46 ± 0.01 *df/f*; $P > 0.05$ and $P < 0.05$, respectively, *t* test), whereas $Arch^-$/$GCaMP^+$ neighboring cells did not have a Ca^{2+} response to the light activation,

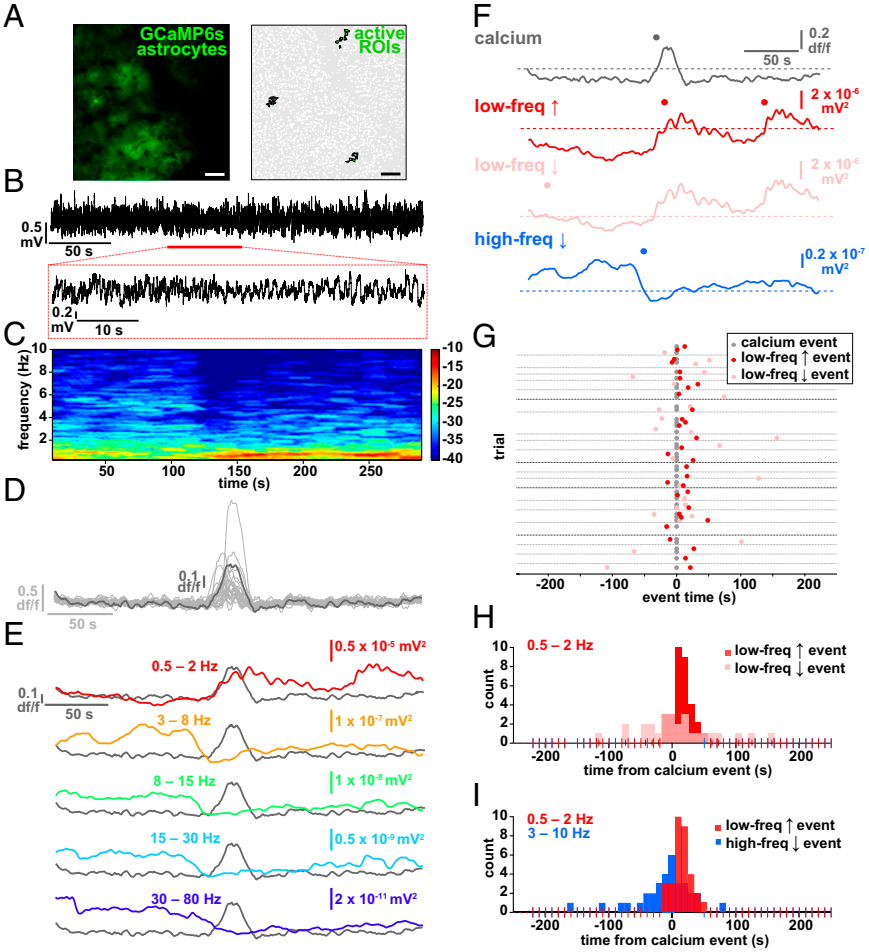

Fig. 2. Astrocyte Ca^{2+} events precede the switch to the slow-oscillation state. (*A*) Astrocyte-specific expression of GCaMP6s (*Left*) and active ROIs (*Right*). (Scale bars, 50 μm.) (*B*) Raw 5-min LFP recording at the site shown in *A*. The expanded area in the red box (*Bottom*) shows an example of a shift to a slow-oscillation–dominated regime. (*C*) Power spectrogram of 0.25- to 10-Hz frequencies in the LFP shown in *B*. Note the transition to the slow-oscillation state (0.5–2 Hz; increase in red). (*D*) Ca^{2+} traces from 22 active ROIs in *A* (light gray) and the average of all traces in dark gray. (*E*) Overlay of astrocyte Ca^{2+} and the mean of frequency change to bands to 80 Hz. (*F*) Automatically detected mean Ca^{2+} (gray), low-frequency (0.5–2 Hz) increase (red) and decrease (pink) events, and high-frequency (3–10 Hz; blue) decrease events (dots) above thresholds (dashed lines). (*G*) All low-frequency LFP events from Ca^{2+} event time. Only the nearest LFP events to the Ca^{2+} event are shown for clarity. Gray dots represent automatically detected average Ca^{2+} events, and red and pink dots show LFP low-frequency increase and decrease events, respectively. Gray horizontal lines separate each 5-min trial. Darker gray lines indicate trials from different animals. (*H*) Distribution of events shown in *G*. (*I*) Distribution of all low-frequency increase events plotted with all high-frequency decrease events from all trials.

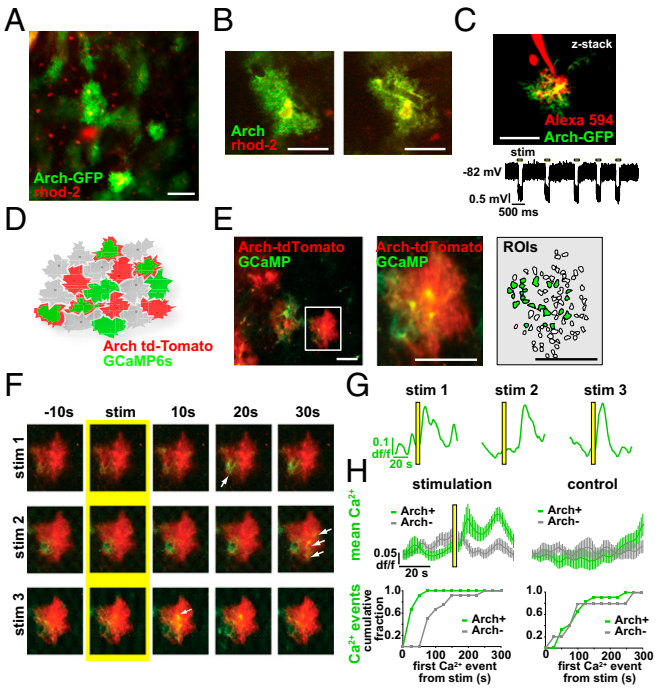

Fig. 3. Optogenetic activation of Archaerhodopsin (Arch) in cortical astrocytes drives Ca^{2+} increases. (*A* and *B*) Astrocyte-specific expression of Arch-GFP (green) throughout the astrocyte processes with stereotyped astrocyte morphology. Astrocyte somata are specifically labeled with rhod-2 (red). (*C*) Astrocyte in cortical slice expressing Arch-GFP and whole-cell patch-clamped with Alexa Fluor 594 in the pipette (*Top*). Yellow light stimulation causes the astrocyte to hyperpolarize (*Bottom*). (*D*) Cartoon of coexpressed astrocytic GCaMP6s and Arch-tdTomato. (*E*) Coexpression of GCaMP6s and Arch-tdTomato in vivo (*Left*), zoomed-in to show a single coexpressing cell (*Middle*), with automatically detected ROIs used for analysis and active ROIs shaded in green (*Right*). (*F*) Three successive stimulation (5-s) trials of the $GCaMP^+/Arch^+$ astrocyte from *E*. Yellow highlights the frame before stimulus onset and white arrows point to GCaMP fluorescence increases in astrocyte processes poststimulus. (*G*) Mean astrocyte Ca^{2+} dynamics in each of the three trials in *F*. Yellow bars denote stimulus throughout the figure. (*H*, *Top*) Average Ca^{2+} across animals in all stimulation (*Left*) and no-stimulation (control; *Right*) trials in $GCaMP^+/Arch^+$ astrocytes (green) and $GCaMP^+/Arch^-$ astrocytes (gray) ± SEM. (*H*, *Bottom*) Time from light stimulus to first Ca^{2+} event, as detected in Fig. 1 in stimulation (*Left*) and control (*Right*) trials. [Scale bars, 50 μm (*A*, *C*, and *E*) and 25 μm (*B*).]

either by mean fluorescence levels (Fig. 3*H*, *Top*) or automatically detected Ca^{2+} events, as in Fig. 1 (Fig. 3*H*, *Bottom*). To further confirm that activation of astrocytes was limited to $Arch^+$ astrocytes and was not due to viral coexpression of two proteins in astrocytes or to the light stimulation itself, we also coexpressed GCaMP6s and tdTomato (without Arch) and performed the same experiments. In these experiments, light activation did not evoke Ca^{2+} transients in the astrocyte branches or processes of $tdTomato^+/GCaMP^+$ astrocytes, nor was Ca^{2+} activity significantly different from neighboring $tdTomato^-/GCaMP^+$ controls (Fig. S4 *E* and *F*; $n = 4$ animals, 28 trials; $P > 0.1$, *t* test, two-sample *F* test).

Interestingly, each 5-s optogenetic activation with Arch (followed by 5 min of imaging and interleaved with a 6-min control trial) evoked Ca^{2+} signals in different branches of each $Arch^+$ astrocyte (Fig. 3*F*, arrows), similar to the spatiotemporal branch specificity of Ca^{2+} changes observed under baseline conditions (33, 34, 40, 47) (Fig. 1 and Movie S2). Astrocytic somata largely did not respond to Arch stimulation, even with visible protein expression there (mean 35.1 ± 9.4 active ROIs in all $Arch^+/GCaMP^+$ astrocytes, 33.2 ± 8.9 active ROIs in processes). Other groups have previously tested optogenetic and nonoptogenetic methods to activate astrocytes by measuring Ca^{2+} increases only in the soma (48–51), even though somatic activity is much more rare under baseline conditions (Fig. 1 *E*–*H*).

We next carried out experiments to investigate the mechanisms by which Arch causes Ca^{2+} increases in astrocyte processes. Because Arch activation causes hyperpolarization of cells, we whole-cell patch-clamped GCaMP6s-expressing astrocytes in slices and imaged the patched cells for hyperpolarization-induced changes in $[Ca^{2+}]_i$ (Fig. 4*A*). Five-second hyperpolarizations (500-ms pulses × 10, mean −15.1 ± 1.2-mV change) were induced to the patched cell, interleaved with control trials. Ca^{2+} levels significantly increased throughout the cell, including processes, following the hyperpolarization compared with control trials (Fig. 4*B*). The voltage changes that caused these Ca^{2+} increases were much larger than those recorded from astrocytic soma during light activation carried out over the entire cell (Fig. 3*C*). However, this is not surprising; due to the low input resistance of astrocytes (20, 52), the voltage change required at the soma to elicit a similar hyperpolarization at the distant processes, where we observe the Ca^{2+} changes following light activation, would need to be higher than we record during light stimulation. Because we can observe hyperpolarization-induced Ca^{2+} increases, our data indicate that hyperpolarization of astrocytes—and its subsequent effects on voltage-dependent channels, receptors, or transporters—may be the mechanism by which Arch stimulation increases $[Ca^{2+}]_i$. While carrying out these experiments, we also found that by using the stereotyped astrocytic electrophysiological marker of network UP states (Fig. 4*C*, *Top*) (20, 43) to monitor population activity in the slice, it was evident that hyperpolarization of single astrocytes not only increased astrocytic Ca^{2+} but also increased the number of UP states in the network in the 100 s following the stimulation compared with control trials (Fig. 4*C*). This result is consistent with our previous work demonstrating that stimulation of a single astrocyte increases the Ca^{2+} activity in the local astrocytic network and leads to increased cortical UP states, which constitute the slow oscillation (20).

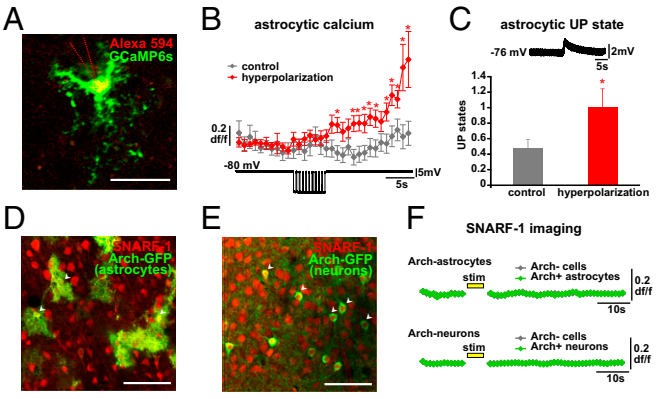

Fig. 4. Mechanisms of Arch activation of astrocytes. (*A*) GCaMP6s-expressing astrocyte (green) under whole-cell patch clamp using a pipette filled with Alexa Fluor 594 (red) to confirm the correct cell. Single two-photon image; the pipette outline is shown with dashed lines because the pipette is out of the optical plane. (Scale bar, 50 μm.) (*B*) GCaMP Ca^{2+} dynamics in patched astrocytes in hyperpolarization (red) and control (gray) trials. Example of astrocyte electrophysiological recording, including hyperpolarization period, shown below Ca^{2+} data (*$P < 0.05$, *t* test; $n =$ 10 cells, 34 110-s paired trials). (*C*, *Top*) Stereotypical astrocytic UP state (20) used to quantify network synchronization following hyperpolarization. (*C*, *Bottom*) Increased UP states following single-astrocyte hyperpolarization from same experiment as in *B*. (*D* and *E*) Two-photon single-plane images of SNARF-1 loading of astrocytes and neurons in slice (red) and specific Arch-GFP expression (green) in either astrocytes (*D*) or neurons (*E*). White arrowheads indicate double-labeled somata of the respective cell types. (Scale bars, 50 μm.) (*F*) SNARF-1 fluorescence dynamics before and after Arch stimulation (yellow bar; 5 s) of astrocytes (*Top*) and neurons (*Bottom*) in $Arch^+$ cells (green) and surrounding $Arch^-$ cells (gray) (astrocytes: $n = 15$ $Arch^+$ cells, 264 $Arch^-$ cells, 8 110-s trials each; neurons: $n = 46$ $Arch^+$ cells, 313 $Arch^-$ cells, 8 110-s trials each). Error bars are ± SEM.

We next addressed potential changes in pH levels in Arch-expressing cells and surrounding Arch$^-$ cells, using the pH indicator SNARF-1 as used in the paper describing neurons (45). We used viral injections to express Arch in either astrocytes (*AAV5-FLEX-ArchT-GFP* into a GFAP-Cre mouse; Fig. 4*D*, green) or neurons (*AAV5-CaMKII-ArchT-GFP* in a WT mouse; Fig. 4*E*, green) and bulk-loaded the slices with SNARF-1, which labels both neurons and astrocytes (Fig. 4 *D* and *E*, red) and exhibits a decrease in fluorescence upon challenge with NH_4Cl, which causes intracellular alkalinization (Fig. S4*G*). Following a 5-s light stimulation of Arch, we observed no significant changes in pH in either the Arch-expressing or the surrounding cells in either case (Fig. 4*F*), consistent with the minimal and fast pH changes observed in neurons following Arch stimulation (45) and in contrast to pH changes observed in cultured astrocytes following Channelrhodopsin [ChR2 (H134R)] activation (53) and in cerebellum Bergmann glia following Arch activation specifically after oxygen and glucose deprivation (54). However, because we could not accurately image pH during the light stimulation itself, we cannot discount any pH changes that may have occurred during this time. Although the exact mechanism of Arch-stimulated Ca^{2+} increase in astrocytes is unclear, we think Arch's hyperpolarizing action represents a good possibility. Further, there are no current tools, to our knowledge, that have been shown to increase Ca^{2+} levels specifically in astrocyte processes with spatiotemporal dynamics similar to spontaneous activity. Thus, Arch activation may be a more physiological method of astrocytic Ca^{2+} activation than has previously been reported.

Astrocyte Activation Leads to a Specific Shift in Low-Frequency Power. With this optogenetic tool in hand, we tested whether the activation of astrocytes affected the low- and high-frequency oscillations measured spontaneously in Figs. 1 and 2. LFP was recorded for 1 min before a 5-s light stimulation of Arch$^+$ astrocytes (confirmed by immunostaining; Fig. S5*A*) and continued for 5 min after the stimulation, with no-stimulation control trials interleaved between each trial (Fig. 5*A*). Following Arch activation, we observed an increase in the power of the low-frequency oscillation that persisted for over a minute, without any significant change in higher frequency bands, indicating that the local network measured by LFP had shifted into a slow-oscillation–dominated regime (Fig. 5 *B–D*; $n = 8$ animals, 28 paired trials). Thus, although we observe astrocyte Ca^{2+} events preceded by decreased high-frequency and followed by increased low-frequency oscillatory activity during spontaneous state shifts (Fig. 2), astrocytic Ca^{2+} manipulation specifically drives the network to the low frequency-dominated state, suggesting that astrocytes are not merely responding to a prior decrease in high-frequency activity and are active drivers of the state change. In addition, these data raise the possibility that the activity changes that occur during state shifts can be mechanistically uncoupled.

In addition to the mean power in each LFP band, we also quantified the data by automatically detecting LFP events (as in Fig. 2*F*) and calculating the time from the stimulation to the first LFP event in the two frequency bands (Fig. S5 *B* and *C*). By this measure, there was also a significant shift earlier in the low-frequency events in each trial compared with control trials (Fig. 5 *E–G* and Fig. S5 *D* and *E*; mean event time from stim 53.6 ± 8.2 s vs. 113.9 ± 14.5 s control; $P < 0.001$, *t* test, two-sample *F* test), whereas there was no shift in the distribution of events in the high-frequency band (Fig. S5 *F* and *G*; mean event time from stim 94.2 ± 15.2 s vs. 101.7 ± 15.9 s control; $P > 0.5$, *t* test, two-sample *F* test). To ensure that the light used for stimulation was not causing the electrophysiological effects, we carried out the same experimental protocol in animals with Arch$^-$/tdTomato$^+$ astrocytes (Fig. S5*H*). In these animals, no significant shift in LFP power was observed in either frequency band (Fig. S5 *I* and *J*; $n =$ 4 animals, 28 trials), nor was there a change in the mean time to the first LFP event (Fig. S5 *K–O*; low-frequency event from stim 80.4 ± 10.4 s vs. 103.4 ± 16.1 s control; $P > 0.1$, *t* test; high-frequency event from stim 109.7 ± 11.4 s vs. 118.5 ± 12.9 s control; $P > 0.5$, *t* test). As a crucial control for any potential nonspecific expression of Arch in neurons, we drove Arch expression specifically in pyramidal neurons in L2/3 using a CaMKII-Arch virus. In this control, light stimulation inhibits Arch$^+$ neurons and, again, we detected no significant change in the slow oscillation following stimulation, indicating that the effects we observe are specifically due to astrocytic—not neuronal—activation (Fig. S6; $n = 4$ animals, 20 trials). Further, these controls also suggest that any brief, circuit-wide decreases in extracellular pH due to Arch-specific H^+ pumping do not cause the slow-oscillation increases observed after astrocyte activation of Arch.

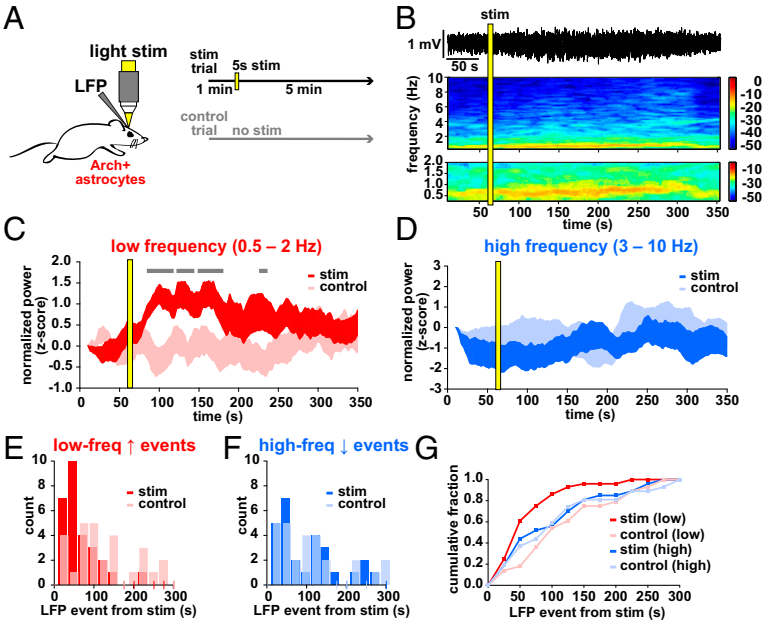

Fig. 5. Arch activation of astrocytes shifts the circuit into a slow-oscillation regime. (*A*) Schematic of the Arch/LFP experiment. Stimulation trials consisted of a 1-min baseline, 5-s stimulation, and 5-min recording, with an interleaved control trial of the same total duration. (*B*) Example LFP recording from a stimulation experiment (*Top*) and the corresponding spectrogram of 0.25–10 Hz (*Middle*) and 0.25–2 Hz (*Bottom*). (*C* and *D*) Normalized (*z*-score) low-frequency (*C*) and high-frequency (*D*) LFP power in stimulation and control trials ±SEM. In *C*, gray bars denote significance compared with controls ($P < 0.05$, *t* test). (*E–G*) Automatically detected low-frequency (0.5–2 Hz; *E*) and high-frequency (3–10 Hz; *F*) LFP events as quantified in previous figures, plotted as time from Arch stimulation to LFP event in stimulation (red and blue) and control (pink and light blue) trials. Events are plotted in 25-s bins, and all conditions are plotted as a cumulative histogram (*G*).

Astrocyte Ca^{2+} Activity Precedes Synchronous Neuronal Firing and Can Drive Coactive Neuronal Events. Because the low frequency-dominated state is characterized by highly synchronous neuronal activity (55), we reasoned that we might uncover the cellular mechanisms by which astrocytes regulate the switch to the slow oscillation by optically monitoring neuronal population activity. To first define baseline astrocyte/neuronal optical activity, we simultaneously imaged Ca^{2+} in neurons and astrocytes with GCaMP6s through a double viral injection of *AAV1-hsyn-GCaMP6s* and *AAV1-CAG.FLEX-GCaMP6s* into an hGFAP-Cre mouse, and could distinguish between these two signals due to their previously characterized temporal dynamical and morphological differences (31, 40) (Fig. 6*A*, Fig. S7 *C* and *D*, and Movie S6). Because some groups have reported faster rise times of astrocytic Ca^{2+} than others (34, 56, 57), we ensured that all ROIs defined as neuronal were contiguous with neuronal cell bodies or showed morphological characteristics distinctive to neurons, including their long dendritic processes. The small population of ambiguous ROIs were eliminated from analysis (*Materials and Methods*). Neurons and their processes regularly exhibit highly synchronized spontaneous Ca^{2+} activity both in vitro and in vivo, under waking and anesthetic conditions, and during synchronized and desynchronized brain states (14, 58) (Fig. 6*B*). When we measure astrocyte Ca^{2+} activity simultaneously, we observe that astrocytic Ca^{2+} begins to increase 4.4 ± 1.0 s before the onset of the synchronous ("coactive") neuronal event (Fig. 6 *C* and *D*; $n = 4$ animals, 15 5-min trials), indicating that astrocyte Ca^{2+} signals precede an optical measure of spontaneous synchronous neuronal activity. We reasoned that because spontaneous astrocyte Ca^{2+} activity preceded coactive neuronal events, coactive neuronal firing might be affected by astrocyte activation, which could help explain the LFP effects we observed in the Arch-activation experiments. Therefore, we tested whether coactive neuronal firing activity at the single-cell level was changed following astrocytic Arch stimulation using a double viral injection to simultaneously express GCaMP6s in neurons and Arch-tdTomato in astrocytes (Fig. 6*E* and Fig. S7*E*). We observed fluctuations in the neuronal GCaMP that reflect spontaneous action potential firing (31) (Fig. 6*F*, *Top*) and quantified coactive neuronal events (Fig. 6*F*, *Bottom*) before and after astrocyte stimulation. Following the stimulation, there were indeed more total action potentials (APs) during the coactive events compared with controls (Fig. 6*G*; $n = 4$ animals, 16 stim trials; $P < 0.05$, t test), an effect most pronounced in the time bin 90 s after the stimulation (Fig. 6*F*, star), a time point where we also observed the greatest shift in low-frequency LFP power in the Arch-LFP experiment (Fig. 5*C*). There was no significant difference in the total number of coactive events, nor in the number of active cells, during each coactive event (Fig. S7 *F–H*; $P > 0.1$, t test), although we did measure an increase in total APs across bins (Fig. S7*H*; $P < 0.05$, t test), consistent with optogenetic activation of astrocytic somata using ChR2 (51). These results suggest that coactive neuronal firing may underlie the increase in the power of the slow oscillation that we observe following Arch stimulation (Fig. 5*C*), indicating that cortical astrocyte activity influences the synchronization of territories of neurons.

Extracellular Glutamate Spikes Co-Occur with Shifts to the Slow-Oscillation State and Can Be Driven by Astrocyte Activation. To investigate the astrocytic signaling mechanisms by which the switch to the slow oscillation may occur, we carried out simultaneous LFP recording and imaging of extracellular glutamate using astrocytic expression of the glutamate sensor GluSnFR (59) (Fig. 7 *A* and *B*) because extracellular glutamate has previously been shown to initiate UP states in slices (20, 60) and because astrocytes are important in the regulation of extracellular glutamate (61). In L2/3, we observe periodic, fast (≤1.5-s) spikes in GluSnFR fluorescence above baseline, which occur widely (1,163.5 ± 61.0 μm^2) and near-simultaneously across an individual astrocyte (Fig. 7 *C* and *D*, cyan; $n = 4$ animals, 22 5-min trials; Movie S7) and faster than the more local and progressive Ca^{2+} activation observed with GCaMP (Fig. 1 and Movies S1 and S2). These glutamate spikes also co-occurred with the low-frequency events, as detected earlier (Fig. 2*F*), with peaks just 1.7 ± 2.03 s before the shifts to the low-frequency regime, whereas there was no clear relationship between glutamate spikes and shifts away from the low-frequency regime (two-sample F test), nor to shifts related to the high frequency (Fig. 7 *D* and *E* and Fig. S8 *A–E*). These results suggest that transient extracellular glutamate increases are involved in the mechanistic shift of the cortical network to the slow oscillation. To test whether Arch stimulation of astrocytes triggers neuronal synchronization through this glutamatergic pathway, we coexpressed GluSnFR and Arch-tdTomato in astrocytes and monitored glutamate spikes following Arch stimulation

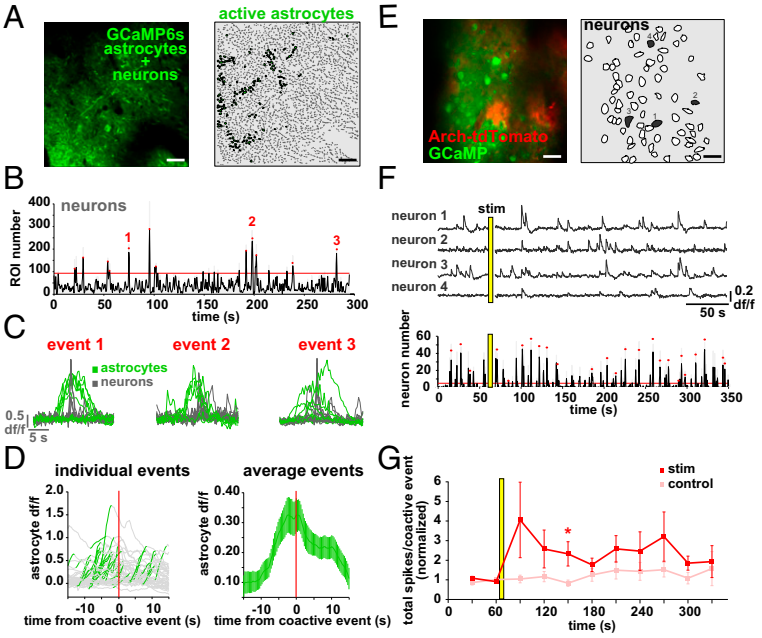

Fig. 6. Astrocytic activity precedes synchronous neuronal events, and Arch activation of astrocytes increases coactive neuronal spiking. (*A*) Simultaneous expression of GCaMP6s in neurons and astrocytes (*Left*) and active astrocytic (green) ROIs (*Right*). (*B*) Large neuronal coactive events (red dots) detected above threshold (red line). No astrocytic ROIs are included in coactive event detection. (*C*) Eleven representative neuronal (gray) and astrocytic (green) ROIs, zoomed-in to display the difference in dynamics between neuronal (gray) and astrocytic (green) ROIs during three representative coactive events. When superimposed, it is evident that slower astrocyte transients precede synchronous neuronal events. (*D*, *Left*) Average of all active astrocytic ROIs 15 s before and after each neuronal coactive event (red line; $n = 45$ events). The increase in each average astrocyte Ca^{2+} is colored green. (*D*, *Right*) Mean ± SEM of astrocyte Ca^{2+} activity around all coactive neuronal events. (*E*) Simultaneous expression of Arch-tdTomato in astrocytes and GCaMP6s in neurons in the same field, with corresponding neuronal ROIs for analysis. (*F*, *Top*) Example Ca^{2+} traces of the four numbered neurons in *E*. (*F*, *Bottom*) Neuronal action potential firing during stimulation trial, with coactive events marked by red dots. (*G*) Average total neuronal firing within all coactive events ± SEM grouped in 30-s bins, normalized to the average in the first two bins (prestim) for stimulated (red) and interleaved control (pink) trials. An asterisk marks the bin with a statistically significant difference between conditions ($P < 0.05$, t test). A yellow bar denotes a 5-s stimulus throughout the figure. (Scale bars, 50 μm.)

(Fig. 7*F*). Indeed, we found that in Arch$^+$/GluSnFR$^+$ astrocytes, the glutamate spikes observed in the 5 min following stimulation were concentrated in the 30–60 s following the stimulation (cyan), whereas in no-stim control trials they were evenly distributed across the trial time (Fig. 7*G*, gray; $n = 5$ animals, 21 trials; two-sample F test), although there was no significant difference in the number of glutamate spikes in each condition (Fig. S8*F*; $P > 0.5$, t test). The area of the fluorescent spike (1,886.7 ± 208.5 control vs. 1,853.8 ± 216.2 μm^2 stim; $P > 0.05$, t test) and the amplitude (0.30 ± 0.04 control vs. 0.26 ± 0.07 d*f*/*f* stim; $P > 0.05$, t test) were not different in stimulation and control trials, indicating that evoked and spontaneous glutamate spikes are equivalent. Although the GluSnFR probe shows pH sensitivity (59), our pH imaging experiments (Fig. 4 *D* and *F*) indicate that the transient change in extracellular pH caused by Arch activation does not persist during the period of increased glutamate spikes, suggesting that the spikes are due to changes in extracellular glutamate itself. These data are consistent with the idea that regulation of extracellular glutamate—via altering the dynamics of astrocytic glutamate transporters, release of glutamate from astrocytes themselves, or by neurons through an indirect astrocyte pathway —is the signaling mechanism that shifts cortical neuronal networks to a low-frequency synchronized state (Fig. 8).

Discussion

Using a combination of optical and electrophysiological techniques, we show that astrocytes in vivo can trigger a switch of the cortical circuit to the slow-oscillation–dominated state. Also, by imaging extracellular astrocytic glutamate with GluSnFR in vivo, we provide evidence consistent with a glutamatergic mechanism of this state switch. Finally, we demonstrate that Arch is a previously unidentified and useful tool for acute optogenetic activation of astrocytes by activating astrocytic processes selectively, at amplitudes and durations similar to physiological levels.

Origins of the Ca^{2+} and Glutamate Events Preceding the Shift to the Slow-Oscillation State. We observe two consistent physiological phenomena in astrocytes in vivo—Ca^{2+} increases in their processes and extracellular glutamate transients—that precede the low frequency-dominated state, implying that the shift to the slow oscillation can be regulated by astrocytic control of extracellular glutamate. Further, we show using optogenetics that astrocyte activation can regulate this cortical state shift. However, many open questions about the role of astrocytic Ca^{2+}, and how control of glutamate levels could lead to the state shift in this circuit, remain. What signals—neuronal or nonneuronal, intra- or extracellular, synchronized or desynchronized—cause the intracellular astrocytic Ca^{2+} rises that occur before the state switch? There has been recent focus on mechanisms of focal Ca^{2+} activation in astrocyte processes, both synaptic and nonsynaptic (30, 33, 34, 47, 62), but no broad consensus yet exists. G protein-coupled receptor (GPCR) activation and release of Ca^{2+} from intercellular stores via IP$_3$ receptors is an accepted pathway for Ca^{2+} increases in astrocyte somata (63, 64), although it has recently been argued that this mechanism may not explain Ca^{2+} increases in astrocyte processes (30). More pharmacological, genetic, and electrophysiological work remains to discover what drives the Ca^{2+} dynamics in astrocytes that are responsible for the subsequent increased low-frequency power. In addition, a broader imaging field, both in the *xy* and *z* planes, could help disambiguate the timing of neuronal and astrocytic Ca^{2+} signaling and address how spatially or temporally localized these transients must be to cause the state switch. Techniques now exist that enable simultaneous imaging in multiple planes (65–68), and multiplane imaging of neurons and astrocytes—while electrophysiologically recording—may give an indication of the spatiotemporal parameters of the events that drive the state change, particularly feedforward or feedback information from other layers in the cortical circuit. One possibility is that L2/3 activation of astrocytes triggers the state switch via their action on synaptic connections between L2/3 neurons and dendrites of L5 neurons, as the slow oscillation has been demonstrated to be generated in L5 (60, 69), and multiplane imaging of both cell types, in both layers, could test this hypothesis.

While Ca^{2+} signals in astrocytes have been intensely studied, there has been little work done on imaging extracellular glutamate around astrocytes. Our description of spontaneous glutamate spikes in vivo

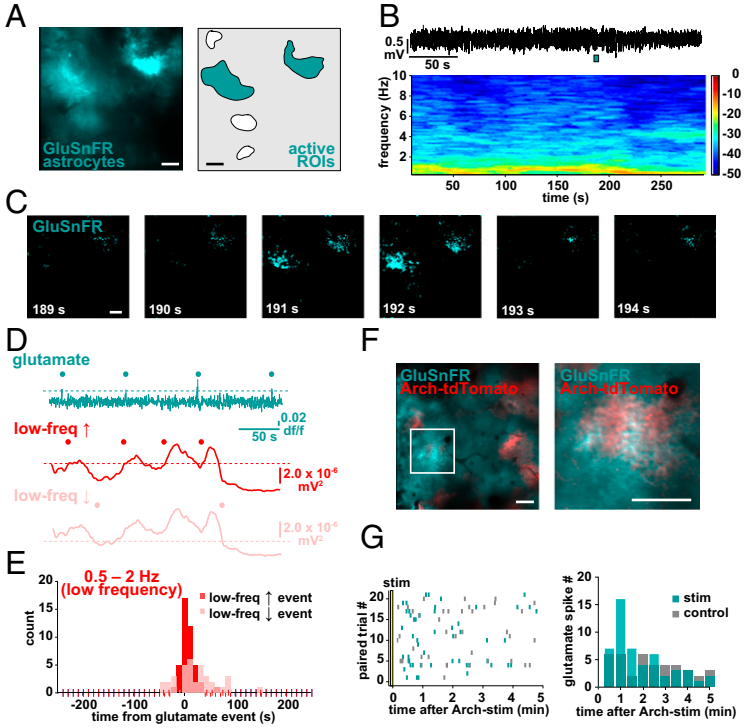

Fig. 7. Astrocytic GluSnFR spikes occur at the switch to the slow oscillation. (*A*) GluSnFR expression in astrocytes in vivo (*Left*) and corresponding ROIs chosen for analysis (*Right*). (*B*) Simultaneous LFP recording (*Top*) and corresponding spectrogram (*Bottom*) during GluSnFR imaging. (*C*) Example of GluSnFR fluorescence throughout two astrocytes in the imaging field in *A*. Images correspond in time to the cyan bar under LFP in *B*, *Top*. (*D*) Glutamate (cyan) and low-frequency increase (red) and decrease (pink) traces and events (dots) from the experiments in *A*–*C*. (*E*) Distribution of LFP events (up, red; down, pink) relative to glutamate spikes (at time 0). (*F*) Astrocytic coexpression of GluSnFR and Arch-tdTomato in vivo. The astrocyte in the white box (*Left*) is magnified (*Right*) to demonstrate the colocalization of proteins on astrocyte processes. (*G*, *Left*) Raster plot of all glutamate spikes in Arch$^+$/GluSnFR$^+$ astrocytes in paired (control, gray; stim, cyan) trials. (*G*, *Right*) Distribution of GluSnFR spikes in paired trials, in 30-s bins. (Scale bars, 50 μm.)

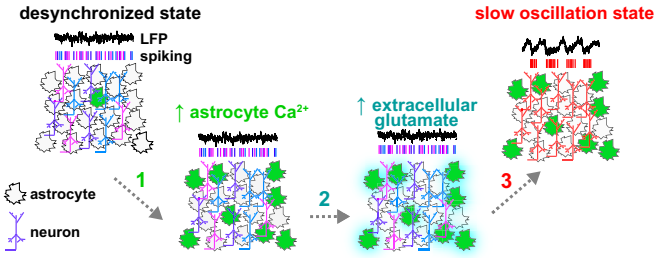

Fig. 8. Model. During desynchronized epochs, populations of neurons do not fire in a coordinated fashion and astrocytic Ca^{2+} signaling is low. Astrocyte Ca^{2+} activity increases in the local circuit through a variety of mechanisms (arrow 1; green), followed by (arrow 2) accumulation of extracellular glutamate (cyan) and a shift (arrow 3) into the slow-oscillation state.

and their close occurrence with shifts to the slow-oscillation state raises intriguing questions about the role of astrocytes in glutamate regulation, a long-standing source of debate. One central issue is whether the source of the glutamate that the astrocytes are sensing is astrocytic or neuronal. Basal glutamatergic synaptic transmission is presumably occurring continually across the thousands of excitatory synapses to which even a single astrocyte has access (24). Why do these large increases in glutamate occur periodically, and what do they reflect? Because the increase in GluSnFR fluorescence occurs largely uniformly across the entire astrocyte and its processes, it may be appealing to assign the source of the glutamate rise to the astrocyte itself. If this were the case, the change could be due to the highly debated gliotransmission (vesicular glutamate release), an inhibition of astrocytic glutamate transporters, or release via the glutamate-permeable Best1 channels, among other mechanisms. On the other hand, groups of neurons—in this or other cell layers—that simultaneously fire and release glutamate presynaptically may also lead to these large extracellular glutamate spikes that are sensed or perhaps even modulated by glutamate transport on astrocytes' morphologically active branches (70–72). Whatever the source of the glutamate, the observation that these spikes occur on average 1 s before the shift to the slow-oscillation–dominated state is consistent with previous work demonstrating that glutamate can drive cortical networks into UP states (20, 60). However, it is important to note that this evidence does not preclude other neurotransmitters or signals from being involved in the state switch. Again, simultaneous imaging of astrocytic glutamate in depth across the cortical layers, combined with pharmacological, genetic, or optogenetic manipulations, may offer clues to the nature of these events.

Astrocytes and Neurons Function Jointly in a Network. In this work, we find a relationship between spontaneous astrocytic Ca^{2+} activity and neural circuit state, as well as between extracellular glutamate and network state. These findings stress the importance of monitoring the activity of both astrocytes and neurons simultaneously when studying populations of these cell types within a neural circuit. Our observations would have been missed if we had only measured the activity of either cell type, or if we had not recorded over the course of many minutes. A small snapshot of either neuronal or astrocytic Ca^{2+} (or glutamate) would miss the causal link between astrocytic and neuronal activity or come to completely different conclusions. Thus, one can only understand the cross-talk between neurons and glia in a network by examining both in the same experiments for long periods of time.

Our conclusions help reconcile previous work that may have implicated astrocytes in the slow oscillation due to nonspecific, neuronal expression of dominant-negative SNARE proteins (21, 22, 25, 26). Here we use a viral injection strategy with GFAP-Cre mice to obtain astrocyte-specific expression, and did not observe any fluorescence in neurons in vivo (Figs. 1–3 and 6), nor in accompanying immunostained sections (Figs. S5 and S7). Critically, we carried out an experiment in which we deliberately expressed Arch in a majority of pyramidal neurons, and found that light stimulation of Arch-expressing neurons did not shift the circuit into an increased low-frequency power. Thus, our results are, in principle, consistent with previous findings about astrocytes' involvement in SWS and the slow oscillation and they are acute manipulations, while the disputed results were obtained via longer-term inactivation of astrocytes via the tetracycline-controlled transcriptional activation system (21, 22).

Significance of Astrocyte Activity in Cortical Circuit Function. Whereas previous work has focused on the mechanisms of SWS or the slow oscillation per se, our current work has broad implications for the role of astrocytes in circuit function and state dynamics. Here we identify a previously unidentified cortical mechanism for the shift to the slow oscillation-dominated regime, a state that has been described in sleeping, waking, and anesthetized mammals. Although many mechanisms have been described for shifting the brain into a more attentive, desynchronized state—such as neuromodulators, sensory input, and running (16, 18, 73–76)—far fewer have been found to consistently shift the cortex into the slow-oscillation state, and it has been considered a default state, brought about by lack of input or attention (77). Here we present evidence that challenges this conception: because astrocyte activity can actively shift the local circuit into a slow-oscillation–dominated state, it's possible that this "resting" state is dynamically controlled and the astrocyte network may be processing specific information to enact these changes. Because responses to external stimuli are enhanced during the desynchronized state (15, 17, 76, 78–80), an active shift to the synchronized state could be a homeostatic-like mechanism to decrease processing and increase restfulness on a cellular or systems level. Due to their syncytial architecture and slower Ca^{2+} signaling, astrocytes may be gathering information from across many cells and synapses at longer timescales than neurons may be able to, to regulate this shift. Thus, it will be important to measure and manipulate astrocytes' activity in a range of vigilance states and behavioral/sensory tasks to fully understand their role in state shifts (27, 28, 29). The causal links between astrocyte activity and circuit function we uncover indicate that astrocytes are actively involved in neural circuits necessary for key brain functions such as sleep, memory, and sensory processing.

Materials and Methods

Animals, Viral Infection, and Craniotomy. All experimental procedures were carried out in accordance with National Institutes of Health and Columbia University institutional animal care guidelines. Animals were housed and maintained in a temperature-controlled environment on a 12-h light–dark cycle, with ad libitum food and water, and imaging/electrophysiology experiments were performed at the same time each day. C57BL/6 mice, or hGFAP-Cre transgenic mice obtained from the Jackson Laboratory [FVB-Tg(GFAP-cre)25Mes/J], age postnatal day (P)40–70, were used for in vivo experiments. For viral infection, P21–40 mice were injected with 100–600 nL total virus (single virus or combination of *AAV1-hsyn-GCaMP6s*, *AAV1-CAG.FLEX-GCaMP6s*, *AAV5-GfaABC1D.Lck-GCaMP6f*, *AAV1-GFAP-iGluSnFR*, *AAV5-FLEX-ArchT-GFP*, *AAV5-CaMKII-ArchT-GFP*, *AAV5-FLEX-ArchT-TdTomato*, or *AAV5-FLEX-TdTomato*) at a rate of 130 nL/min at 200 μm from the pial surface of the visual cortex (x –0.22, y –0.31) using a UMP3 microsyringe pump (World Precision Instruments). Mice were used for in vivo imaging and electrophysiology experiments 2–4 wk postinjection. For slice experiments, viral injection was performed on late P0–early P1 pups with 500 nL total virus at a depth of 200 μm into the assumed V1 and used for experiments at P13–20.

On the in vivo experimental day, mice were anesthetized with urethane (i.p. injection, 1.7 g/kg) and a titanium headplate was attached to the skull using cyanoacrylate glue. A 2 × 2-mm craniotomy, centered on the viral injection site in V1, was performed using a dental drill, leaving the dura intact. A silver wire was attached to a bone screw in the anterior skull for the LFP ground, and both the headplate and bone screw were then attached to the skull using dental cement. Custom-made light-blocking goggles of Buna-N O rings glued to blackout fabric were placed over the eyes and sealed using vacuum grease. In animals used for the isoflurane experiment shown, the procedure was the same except that 2% isoflurane was administered to the animal through a nosepiece during surgery,

and this level was reduced to 0.8–1.0% during the recording. For awake animals, mice underwent training for 1–2 h/d for 2 d on a spherical treadmill with head fixation before recording.

Two-Photon in Vivo Ca^{2+} Imaging, Electrophysiology, and Optogenetic Stimulation. For rhod-2 (rhod-2 AM; Life Technologies) Ca^{2+} imaging experiments, dye was first dissolved in 4 μL freshly prepared DMSO containing 20% Pluronic F-127 (Molecular Probes) and further diluted in 35 μL dye buffer (150 mM NaCl, 2.5 mM KCl, and 10 mM Hepes, pH 7.4). The dye solution was pressure-injected at 150–200 μm at a 30° angle with a glass micropipette (4–7 MΩ, 10 psi, 8 min) under visual control by two-photon imaging. Astrocytic or neuronal activity in layer 2/3 of the visual cortex using rhod-2, GCaMP6s, or GluSnFR was monitored by imaging fluorescence dynamics with a Sutter Movable Objective Microscope (MOM) and a mode-locked dispersion-precompensated Ti:sapphire laser (Chameleon Vision II; Coherent) at 850 nm (rhod-2), 950 nm (GCaMP, SNARF-1), 900 nm (Arch-GFP), 910 nm (GluSnFR), or 1,040 nm (Arch-tdTomato and tdTomato) with a 25× (1.05 N.A.; Olympus) water-immersion objective; 535/50 (GCaMP, Arch-GFP, GluSnFR), 610/75 (Arch-tdTomato, tdTomato, rhod-2), and 572/28 (SNARF-1) emission filters were used. Scanning and image acquisition were carried out at 1, 3, or 4 Hz at 512 × 512 pixels using Sutter software (MScan). Simultaneous LFP measurements were acquired at 1 kHz, using a glass micropipette (2–5 MΩ) filled with saline and lowered to ∼150 μm below the pial surface directly below the imaging plane. LFP signals were amplified and band pass-filtered at 100 Hz. The cranial window was then filled with a premelted 2% agarose solution. Optogenetic activation of $Arch^+$ astrocytes was carried out using wide-field fluorescence (Lambda LS xenon arc lamp; Sutter) through a 550-nm excitation filter.

Slice Preparation, Electrophysiology, and Two-Photon Imaging. Coronal neocortical slices (400-μm-thick) from P14–18 mice were cut with a vibratome (VT1200 S; Leica) in an ice-cold cutting solution of 27 mM $NaHCO_3$, 1.5 mM NaH_2PO_4, 222 mM sucrose, 2.6 mM KCl, 2 mM $MgSO_4$, and 2 mM $CaCl_2$. Slices were incubated for 30 min at 32 °C in standard, continuously aerated (95% O_2/5% CO_2) artificial cerebrospinal fluid (ACSF) containing 123 mM NaCl, 3 mM KCl, 26 mM $NaHCO_2$, 1 mM NaH_2PO_4, 10 mM dextrose, 2 mM $CaCl_2$, and 2 mM $MgSO_4$. Experiments were performed in continuously aerated, standard ACSF. Whole-cell patch-clamp recording of $Arch^+$ astrocytes was performed as previously, using electrodes with a resistance of 6–8 MΩ and an intracellular solution containing 135 mM K-methylsulfate, 10 mM KCl, 10 mM Hepes, 5 mM NaCl, 2.5 mM Mg-ATP, 0.3 mM Na-GTP, and 200 μM Alexa Fluor 594 (20). Two-photon imaging of slices was performed on a custom-made two-photon microscope (81) with a tunable Ti:sapphire laser (Chameleon Ultra; Coherent) and a 40×, 0.8 N.A. objective; 900-nm excitation wavelength and 510/40 (Arch-GFP) and 605/20 (Alexa Fluor 594) emission filters were used. Arch-GFP^+ astrocytes were optogenetically activated with wide-field fluorescence through a 550-nm excitation filter.

Bulk Dye Loading of Slices. For SNARF-1 AM loading, we deposited slices in a petri dish (35 × 10 mm) with 2 mL ACSF. An aliquot of 50 μg SNARF-1 AM (Life Technologies) was prepared in 10 μL DMSO and 2 μL Pluronic F-127 (Invitrogen), shaken for 5 min, and pipetted into the solution. The dish was ventilated with 95% O_2/5% CO_2 and affixed to the bottom of a larger petri dish kept humid with a wet Kimwipe and placed in a 37-°C slide warmer for 25 min. Slices were transferred back into the incubation chamber until experiments were performed.

Immunohistochemistry. Virus-injected mice were anesthetized and perfused transcardially with 4% paraformaldehyde in 0.1 M phosphate buffer (PB; pH 7.4). Brains were removed and postfixed overnight in 4% paraformaldehyde, followed by cryoprotection in 30% sucrose in 0.1 M PB for 48 h at 4 °C. A cryostat (CM3050 S; Leica) was used to cut 40-μm-thick sections from the visual cortex at the injection site. Corresponding sections from the noninjected hemispheres of each brain were cut as controls. Sections were blocked for 30 min at room temperature (RT) in a solution of 0.3% Triton X-100 (Sigma) and 20% normal goat serum (Sigma) in 0.1 M PB. Primary antibodies (rabbit anti-GFAP, 1:500, Abcam; chicken anti-GFP, 1:1,000, Abcam; guinea pig anti-tdTomato, gift of S. Sternson, Janelia Farm, Ashburn, VA) were added and slices were incubated overnight at 4 °C. Slices were washed three times in PB and incubated with secondary antibodies (Alexa Fluor 488 goat anti-chicken; Alexa Fluor 568 goat anti-rabbit; Alexa Fluor 647 goat anti-guinea pig; all 1:500, Invitrogen) for 2 h at RT. Slices were washed in PB and mounted on slides with Fluoromount. Images from injected and control sections were acquired on a confocal microscope (Olympus IX81) with a 10×, 0.4 N.A. objective.

Image Analysis. Initial image processing was carried out using custom-written software in MATLAB (MathWorks) (Caltracer3). Astrocytic ROIs were detected using an automated algorithm based on fluorescence intensity, size, and shape. "Active" astrocytic ROIs were detected using an automated rising-faces algorithm, selecting those ROIs with signals above 0.03 d*f* and three times the noise of each individual trace. Pixels within each ROI were averaged and d*f*/*f* was calculated by dividing each value by the mean of the values from the previous 30 s. Neuronal cell bodies were detected using an automated algorithm and adjusted by visual inspection. Pixels within each neuron were averaged and d*f*/*f* was calculated using the values from the previous 5-s window. Neuronal spike probability was inferred from Ca^{2+} signals using a fast, nonnegative deconvolution method (82). Binary spike activity data were used for neuronal analyses. This method likely underestimates action potentials, particularly when neurons fire a single action potential or at high frequencies. Coactive events were automatically detected based on the binary spike data, using the findpeaks function in MATLAB and excluding any peaks within 10 frames (at 3 Hz) of the coactive event. Trials with motion artifacts were excluded from analysis. For GluSnFR analysis, images were filtered with a median filter (5 pixels), and the average background was subtracted from the filtered image. GluSnFR events are defined by frames that are 3 SDs above the mean of the fluorescence trace. Average area for GluSnFR activations was calculated on the raw images, not the median-filtered images.

For simultaneous neuronal and astrocytic GCaMP imaging, ROIs were detected as described above for astrocytes only, resulting in both neurons and astrocytes divided into many ROIs. ROIs were classified as astrocytic and neuronal based on spatiotemporal dynamics. Neuronal transients were temporally asymmetrical, with short (<1 s) rise times and longer decay times [Fig. S7*D* (31)], whereas astrocytic transients exhibited symmetrical rise and decay times, with longer total duration [Fig. S7 (20, 33)]. In addition, astrocytic transients can radiate across processes in a temporal progression, whereas neuronal transients occurred near-simultaneously across contiguous regions of the—morphologically distinct from astrocytes—cells. In a subset of experiments, astrocyte identity and the spatiotemporal discrimination method were confirmed using rhod-2 labeling of the astrocytic soma. ROIs not clearly classified as astrocytic or neuronal made up a small subset of the total ROIs (<2%) and were not included in the analysis. For each neuronal coactive event, all active astrocyte activity within a 15-s window was averaged. Averaged astrocyte events longer than 1 s and greater than mean +4 SD are used in the total average.

LFP and Astrocyte Ca^{2+} Analysis. Spectral analysis of LFP data was carried out using the Chronux toolbox (chronux.org), using a time frequency bandwidth of 2.5 with four tapers and a 20-s window moving at 0.5-s increments. The mean value within each frequency band was calculated. Ca^{2+} and LFP events were automatically selected by taking the mean of each measure +1 SD (Ca^{2+}) and +0.5 or −0.5 SD (LFP low- and high-frequency bands, respectively), provided the trace stayed above/below this level for at least 8 s. LFP changes based on *z* score (Fig. 3) were calculated using the SD of a 5-min baseline recording immediately before the first optogenetic stimulation trial.

ACKNOWLEDGMENTS. We thank Yeonsook Shin, Alexa Semonche, Kasra Manoocheri, William Snider, and Azadeh Hamzeehei Sichani for technical support; and Ben Shababo, Jesse Jackson, and Inbal Ayzenshtat for assistance with analysis; and members of the R.Y. laboratory for helpful discussions. The project was supported by grants from the National Institute on Drug Abuse (5R21DA034195-02) and the National Institute of Mental Health (1R01MH101218-01) (to R.Y.) and by a Charles H. Revson Senior Fellowship in the Life Sciences (to K.E.P.).

1. Steriade M, Nuñez A, Amzica F (1993) A novel slow (< 1 Hz) oscillation of neocortical neurons in vivo: Depolarizing and hyperpolarizing components. *J Neurosci* 13(8):3252–3265.
2. Hughes SW, Cope DW, Blethyn KL, Crunelli V (2002) Cellular mechanisms of the slow (<1 Hz) oscillation in thalamocortical neurons in vitro. *Neuron* 33(6):947–958.
3. Isomura Y, et al. (2006) Integration and segregation of activity in entorhinal-hippocampal subregions by neocortical slow oscillations. *Neuron* 52(5):871–882.
4. Ji D, Wilson MA (2007) Coordinated memory replay in the visual cortex and hippocampus during sleep. *Nat Neurosci* 10(1):100–107.
5. Steriade M, Timofeev I, Grenier F (2001) Natural waking and sleep states: A view from inside neocortical neurons. *J Neurophysiol* 85(5):1969–1985.
6. Petersen CC, Hahn TT, Mehta M, Grinvald A, Sakmann B (2003) Interaction of sensory responses with spontaneous depolarization in layer 2/3 barrel cortex. *Proc Natl Acad Sci USA* 100(23):13638–13643.
7. Okun M, Naim A, Lampl I (2010) The subthreshold relation between cortical local field potential and neuronal firing unveiled by intracellular recordings in awake rats. *J Neurosci* 30(12):4440–4448.
8. Luczak A, Barthó P, Harris KD (2009) Spontaneous events outline the realm of possible sensory responses in neocortical populations. *Neuron* 62(3):413–425.
9. Nir Y, et al. (2011) Regional slow waves and spindles in human sleep. *Neuron* 70(1):153–169.
10. Vyazovskiy VV, et al. (2011) Local sleep in awake rats. *Nature* 472(7344):443–447.

11. Steriade M, Nuñez A, Amzica F (1993) Intracellular analysis of relations between the slow (< 1 Hz) neocortical oscillation and other sleep rhythms of the electroencephalogram. *J Neurosci* 13(8):3266–3283.
12. Amzica F, Steriade M (1995) Disconnection of intracortical synaptic linkages disrupts synchronization of a slow oscillation. *J Neurosci* 15(6):4658–4677.
13. Timofeev I, Grenier F, Bazhenov M, Sejnowski TJ, Steriade M (2000) Origin of slow cortical oscillations in deafferented cortical slabs. *Cereb Cortex* 10(12):1185–1199.
14. Cossart R, Aronov D, Yuste R (2003) Attractor dynamics of network UP states in the neocortex. *Nature* 423(6937):283–288.
15. Zagha E, Casale AE, Sachdev RN, McGinley MJ, McCormick DA (2013) Motor cortex feedback influences sensory processing by modulating network state. *Neuron* 79(3):567–578.
16. Pinto L, et al. (2013) Fast modulation of visual perception by basal forebrain cholinergic neurons. *Nat Neurosci* 16(12):1857–1863.
17. Bermudez Contreras EJ, et al. (2013) Formation and reverberation of sequential neural activity patterns evoked by sensory stimulation are enhanced during cortical desynchronization. *Neuron* 79(3):555–566.
18. Poulet JF, Fernandez LM, Crochet S, Petersen CC (2012) Thalamic control of cortical states. *Nat Neurosci* 15(3):370–372.
19. Reimer J, et al. (2014) Pupil fluctuations track fast switching of cortical states during quiet wakefulness. *Neuron* 84(2):355–362.
20. Poskanzer KE, Yuste R (2011) Astrocytic regulation of cortical UP states. *Proc Natl Acad Sci USA* 108(45):18453–18458.
21. Halassa MM, et al. (2009) Astrocytic modulation of sleep homeostasis and cognitive consequences of sleep loss. *Neuron* 61(2):213–219.
22. Fellin T, et al. (2009) Endogenous nonneuronal modulators of synaptic transmission control cortical slow oscillations in vivo. *Proc Natl Acad Sci USA* 106(35):15037–15042.
23. Wang F, Xu Q, Wang W, Takano T, Nedergaard M (2012) Bergmann glia modulate cerebellar Purkinje cell bistability via Ca^{2+}-dependent K^+ uptake. *Proc Natl Acad Sci USA* 109(20):7911–7916.
24. Bushong EA, Martone ME, Jones YZ, Ellisman MH (2002) Protoplasmic astrocytes in CA1 stratum radiatum occupy separate anatomical domains. *J Neurosci* 22(1):183–192.
25. Fujita T, et al. (2014) Neuronal transgene expression in dominant-negative SNARE mice. *J Neurosci* 34(50):16594–16604.
26. Sloan SA, Barres BA (2014) Looks can be deceiving: Reconsidering the evidence for gliotransmission. *Neuron* 84(6):1112–1115.
27. Lee HS, et al. (2014) Astrocytes contribute to gamma oscillations and recognition memory. *Proc Natl Acad Sci USA* 111(32):E3343–E3352.
28. Ding F, et al. (2013) α1-Adrenergic receptors mediate coordinated Ca^{2+} signaling of cortical astrocytes in awake, behaving mice. *Cell Calcium* 54(6):387–394.
29. Paukert M, et al. (2014) Norepinephrine controls astroglial responsiveness to local circuit activity. *Neuron* 82(6):1263–1270.
30. Shigetomi E, Tong X, Kwan KY, Corey DP, Khakh BS (2011) TRPA1 channels regulate astrocyte resting calcium and inhibitory synapse efficacy through GAT-3. *Nat Neurosci* 15(1):70–80.
31. Chen TW, et al. (2013) Ultrasensitive fluorescent proteins for imaging neuronal activity. *Nature* 499(7458):295–300.
32. Kanemaru K, et al. (2014) In vivo visualization of subtle, transient, and local activity of astrocytes using an ultrasensitive Ca(2+) indicator. *Cell Reports* 8(1):311–318.
33. Haustein MD, et al. (2014) Conditions and constraints for astrocyte calcium signaling in the hippocampal mossy fiber pathway. *Neuron* 82(2):413–429.
34. Di Castro MA, et al. (2011) Local Ca^{2+} detection and modulation of synaptic release by astrocytes. *Nat Neurosci* 14(10):1276–1284.
35. Otsu Y, et al. (2015) Calcium dynamics in astrocyte processes during neurovascular coupling. *Nat Neurosci* 18(2):210–218.
36. Reeves AM, Shigetomi E, Khakh BS (2011) Bulk loading of calcium indicator dyes to study astrocyte physiology: Key limitations and improvements using morphological maps. *J Neurosci* 31(25):9353–9358.
37. Hirase H, Qian L, Barthó P, Buzsáki G (2004) Calcium dynamics of cortical astrocytic networks in vivo. *PLoS Biol* 2(4):E96.
38. Bonder DE, McCarthy KD (2014) Astrocytic Gq-GPCR-linked IP3R-dependent Ca^{2+} signaling does not mediate neurovascular coupling in mouse visual cortex in vivo. *J Neurosci* 34(39):13139–13150.
39. Ortinski PI, et al. (2010) Selective induction of astrocytic gliosis generates deficits in neuronal inhibition. *Nat Neurosci* 13(5):584–591.
40. Shigetomi E, et al. (2013) Imaging calcium microdomains within entire astrocyte territories and endfeet with GCaMPs expressed using adeno-associated viruses. *J Gen Physiol* 141(5):633–647.
41. Pagliardini S, Gosgnach S, Dickson CT (2013) Spontaneous sleep-like brain state alternations and breathing characteristics in urethane anesthetized mice. *PLoS One* 8(7):e70411.
42. Murakami M, Kashiwadani H, Kirino Y, Mori K (2005) State-dependent sensory gating in olfactory cortex. *Neuron* 46(2):285–296.
43. Mishima T, Hirase H (2010) In vivo intracellular recording suggests that gray matter astrocytes in mature cerebral cortex and hippocampus are electrophysiologically homogeneous. *J Neurosci* 30(8):3093–3100.
44. Gervasoni D, et al. (2004) Global forebrain dynamics predict rat behavioral states and their transitions. *J Neurosci* 24(49):11137–11147.
45. Chow BY, et al. (2010) High-performance genetically targetable optical neural silencing by light-driven proton pumps. *Nature* 463(7277):98–102.
46. Takano T, et al. (2006) Astrocyte-mediated control of cerebral blood flow. *Nat Neurosci* 9(2):260–267.
47. Panatier A, et al. (2011) Astrocytes are endogenous regulators of basal transmission at central synapses. *Cell* 146(5):785–798.
48. Gourine AV, et al. (2010) Astrocytes control breathing through pH-dependent release of ATP. *Science* 329(5991):571–575.
49. Gradinaru V, Mogri M, Thompson KR, Henderson JM, Deisseroth K (2009) Optical deconstruction of parkinsonian neural circuitry. *Science* 324(5925):354–359.
50. Agulhon C, Fiacco TA, McCarthy KD (2010) Hippocampal short- and long-term plasticity are not modulated by astrocyte Ca^{2+} signaling. *Science* 327(5970):1250–1254.
51. Perea G, Yang A, Boyden ES, Sur M (2014) Optogenetic astrocyte activation modulates response selectivity of visual cortex neurons in vivo. *Nat Commun* 5:3262.
52. McKhann GM, II, D'Ambrosio R, Janigro D (1997) Heterogeneity of astrocyte resting membrane potentials and intercellular coupling revealed by whole-cell and gramicidin-perforated patch recordings from cultured neocortical and hippocampal slice astrocytes. *J Neurosci* 17(18):6850–6863.
53. Tang F, et al. (2014) Lactate-mediated glia-neuronal signalling in the mammalian brain. *Nat Commun* 5:3284.
54. Beppu K, et al. (2014) Optogenetic countering of glial acidosis suppresses glial glutamate release and ischemic brain damage. *Neuron* 81(2):314–320.
55. Volgushev M, Chauvette S, Mukovski M, Timofeev I (2006) Precise long-range synchronization of activity and silence in neocortical neurons during slow-wave oscillations [corrected]. *J Neurosci* 26(21):5665–5672.
56. Lind BL, Brazhe AR, Jessen SB, Tan FC, Lauritzen MJ (2013) Rapid stimulus-evoked astrocyte Ca^{2+} elevations and hemodynamic responses in mouse somatosensory cortex in vivo. *Proc Natl Acad Sci USA* 110(48):E4678–E4687.
57. Nizar K, et al. (2013) In vivo stimulus-induced vasodilation occurs without IP3 receptor activation and may precede astrocytic calcium increase. *J Neurosci* 33(19):8411–8422.
58. Gonçalves JT, Anstey JE, Golshani P, Portera-Cailliau C (2013) Circuit level defects in the developing neocortex of Fragile X mice. *Nat Neurosci* 16(7):903–909.
59. Marvin JS, et al. (2013) An optimized fluorescent probe for visualizing glutamate neurotransmission. *Nat Methods* 10(2):162–170.
60. Sanchez-Vives MV, McCormick DA (2000) Cellular and network mechanisms of rhythmic recurrent activity in neocortex. *Nat Neurosci* 3(10):1027–1034.
61. Parpura V, Verkhratsky A (2012) Astrocytes revisited: Concise historic outlook on glutamate homeostasis and signaling. *Croat Med J* 53(6):518–528.
62. Hirase H, Iwai Y, Takata N, Shinohara Y, Mishima T (2014) Volume transmission signalling via astrocytes. *Philos Trans R Soc Lond B Biol Sci* 369(1654):20130604.
63. Porter JT, McCarthy KD (1996) Hippocampal astrocytes in situ respond to glutamate released from synaptic terminals. *J Neurosci* 16(16):5073–5081.
64. Fiacco TA, McCarthy KD (2006) Astrocyte calcium elevations: Properties, propagation, and effects on brain signaling. *Glia* 54(7):676–690.
65. Quirin S, Peterka DS, Yuste R (2013) Instantaneous three-dimensional sensing using spatial light modulator illumination with extended depth of field imaging. *Opt Express* 21(13):16007–16021.
66. Cheng A, Gonçalves JT, Golshani P, Arisaka K, Portera-Cailliau C (2011) Simultaneous two-photon calcium imaging at different depths with spatiotemporal multiplexing. *Nat Methods* 8(2):139–142.
67. Chia TH, Levene MJ (2009) Microprisms for in vivo multilayer cortical imaging. *J Neurophysiol* 102(2):1310–1314.
68. Abrahamsson S, et al. (2013) Fast multicolor 3D imaging using aberration-corrected multifocus microscopy. *Nat Methods* 10(1):60–63.
69. Beltramo R, et al. (2013) Layer-specific excitatory circuits differentially control recurrent network dynamics in the neocortex. *Nat Neurosci* 16(2):227–234.
70. Bellesi M, de Vivo L, Tononi G, Cirelli C (2015) Effects of sleep and wake on astrocytes: Clues from molecular and ultrastructural studies. *BMC Biol* 13:66.
71. Pannasch U, et al. (2014) Connexin 30 sets synaptic strength by controlling astroglial synapse invasion. *Nat Neurosci* 17(4):549–558.
72. Bernardinelli Y, et al. (2014) Activity-dependent structural plasticity of perisynaptic astrocytic domains promotes excitatory synapse stability. *Curr Biol* 24(15):1679–1688.
73. Constantinople CM, Bruno RM (2011) Effects and mechanisms of wakefulness on local cortical networks. *Neuron* 69(6):1061–1068.
74. Niell CM, Stryker MP (2010) Modulation of visual responses by behavioral state in mouse visual cortex. *Neuron* 65(4):472–479.
75. Polack PO, Friedman J, Golshani P (2013) Cellular mechanisms of brain state-dependent gain modulation in visual cortex. *Nat Neurosci* 16(9):1331–1339.
76. Bennett C, Arroyo S, Hestrin S (2013) Subthreshold mechanisms underlying state-dependent modulation of visual responses. *Neuron* 80(2):350–357.
77. Lee SH, Dan Y (2012) Neuromodulation of brain states. *Neuron* 76(1):209–222.
78. Zhuang J, et al. (2014) Brain state effects on layer 4 of the awake visual cortex. *J Neurosci* 34(11):3888–3900.
79. Fu Y, et al. (2014) A cortical circuit for gain control by behavioral state. *Cell* 156(6):1139–1152.
80. Froudarakis E, et al. (2014) Population code in mouse V1 facilitates readout of natural scenes through increased sparseness. *Nat Neurosci* 17(6):851–857.
81. Nikolenko V, Poskanzer KE, Yuste R (2007) Two-photon photostimulation and imaging of neural circuits. *Nat Methods* 4(11):943–950.
82. Vogelstein JT, et al. (2010) Fast nonnegative deconvolution for spike train inference from population calcium imaging. *J Neurophysiol* 104(6):3691–3704.